Acta Materialia 272 (2024) 119899

Contents lists available at ScienceDirect

Acta Materialia

journal homepage: www.elsevier.com/locate/actamat

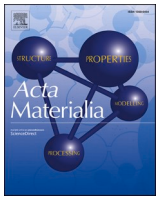

Dynamic evolution of internal stress, grain growth, and crystallographic texture in arc-evaporated AlTiN thin films using in-situ synchrotron x-ray diffraction

Sanjay Nayak [a,*], Tun-Wei Hsu [a], Robert Boyd [a], Jens Gibmeier [b], Norbert Schell [c], Jens Birch [a], Lina Rogström [a], Magnus Odén [a]

[a] Department of Physics, Chemistry and Biology (IFM), Linköping University, SE-581 83 Linköping, Sweden
[b] Institute for Applied Materials, Materials Science and Engineering (IAM-WK), Karlsruhe Institute of Technology, 76131 Karlsruhe, Germany
[c] Helmholtz-Zentrum Hereon, Institute of Materials Physics, Max-Planck-Str. 1, 21502 Geesthacht, Germany

ARTICLE INFO

Keywords:
Insitu XRD
Stress evolution
Texture evolution
AlTiN
Grain evolution

ABSTRACT

Understanding the nucleation and growth of polycrystalline thin films is a long-standing goal. Numerous studies have been done to determine the grain size, stress, and the ideal crystallographic orientation in films. The majority of past studies have either employed an ex-situ methodology or only monitor the development of macroscopic stress in real-time. There has never been any research done on the simultaneous changes in crystallographic texture, grain size, and microscopic stress in polycrystalline thin films. In this study, we investigated the generation and temporal evolution of texture, grain size, and internal stress in cathodic arc evaporated $Al_{0.50}Ti_{0.50}N$ thin films using a bespoke deposition apparatus designed for use with 2-dimensional synchrotron x-ray diffraction technique. The influence of the substrate temperature is investigated in terms of the emergence and development of texture, grain size and stress evolution. A dynamic evolution of the crystallographic texture is observed as the overall film thickness varies. We clearly resolved two regime of films growth based on stress evolution. Beyond a threshold grain size (~ 14 nm), the stress scales inversely to the average grain sizes, and as the film thickness increases, immediate compressive stress relaxation was seen. An extensive ex-situ evaluation of thin films using electron microscopies and electron diffraction was performed to support the in-situ x-ray diffraction results.

1. Introduction

Transition metal nitrides (TMNs), especially AlN-alloyed TiN ($Al_xTi_{1-x}N$)-based thin films, show extraordinary physical, mechanical, and tribological properties, e.g., high mechanical hardness, high melting temperature, thermodynamic stability at elevated temperature, and oxidation resistance [1,2]. Owing to these characteristics, thin films of $Al_xTi_{1-x}N$ are preferred as protective films that extend the life of cutting tools and inhibit corrosion. In practice, polycrystalline thin films of $Al_xTi_{1-x}N$ are deposited on top of a rigid substrate (e.g., cutting tools) by physical vapour deposition (PVD), such as magnetron sputtering or cathodic arc evaporation, or chemical vapour deposition (CVD) techniques. Typical PVD deposited films possess nanocolumnar and/or nanocrystalline morphologies [3] with preferred orientation of certain crystallographic planes along the growth direction (known as crystallographic texture). As the PVD deposition involves non-equilibrium processes and the formation of high-energy ions, as-deposited films are also often in a state of residual stress. These inherent stresses (usually compressive stresses) in PVD coated thin films play a vital role in the overall performance and efficiency of the films. During mechanical operations, the stress due to external mechanical loads adds to the pre-existing stress. A high pre-existing stress may lead to the complete failure of the coating, including its delamination from the substrate. At the same time the smaller values of residual stress and low values of mechanical hardness correlate with each other [4,5]. Thus, optimizing the stress in thin films is important and it is required for industry to realize their full potential. In this regard understanding the mechanisms of thin film nucleation and growth has been an important aspect of research for the community, since these factors are essential in determining the properties of films and their practical significance.

* Corresponding author.
E-mail addresses: sanjaynayak.physu@gmail.com, sanjay.nayak@liu.se (S. Nayak).

https://doi.org/10.1016/j.actamat.2024.119899
Received 26 January 2024; Received in revised form 26 March 2024; Accepted 4 April 2024
Available online 5 April 2024

It has already been established that many process parameters in PVD can be used to tune the film's stress level. For example, application of a negative substrate bias voltage (V_s) leads to the formation of finer grains and an increase in residual stress [6–9]. At the same time, higher V_s also helps in the deposition of dense or compact films and leads to high mechanical hardness. The partial pressure of N_2 in the total growth pressure ($Ar+N_2$) influences the composition, roughness, grain size, and microstructure of the films. The non-stoichiometric films, resulting from different $Ar+N_2$ combinations, show poor mechanical hardness [10–13]. Machet et al. [14] examined the effect of substrate temperature (varying from 100 °C to 450 °C) on the elemental composition, surface morphology, and mechanical hardness properties of magnetron sputtered TiN films. They found that for a given N_2 partial pressure, the development of crystallographic texture is greatly influenced by the substrate temperature. At low growth temperatures (below 300 °C), 111 crystallographic texture of the face-centered-cubic (FCC) TiN phase forms in the growth direction (GD), while at higher temperature a 200 and/or 220 texture of FCC-TiN are developed along GD. Machet et al. [15] characterized the mechanical properties of the films and claimed that TiN films with a crystallographic texture of 111 possess a hardness of 20 GPa, but exhibit poorer wear resistance than films with a crystallographic texture of 200, which have a hardness of 25 GPa along with a good wear resistance. A similar observation was made by Wang et al. [16] in (Ti, Al)N films deposited with cathode discharge deposition process. Kalss et al. [17] investigated the interdependence of stress and crystallographic texture in (Al, Ti)N films deposited with cathodic arc evaporations and argued that the formation of high index crystallographic plane's texture (e.g., 113 and 115) leads to residual stress relaxation and reduction in film density, contrary to Beckers et al. [18] and Greene et al. [19].

Most of the above-mentioned reports determined residual stress (or simply stress), crystallographic texture, and grain size after the film's deposition and after cooling down from growth to room temperature. Little is known about the real-time formation and evolution of stress and microstructure of $Al_xTi_{1-x}N$ thin films, particularly when deposited with the industry-preferred arc evaporation technique. Recently, by utilizing a home designed cathodic arc evaporation chamber [20], adapted for in-situ synchrotron radiation studies, we recorded the evolution of stress/strain and microstructure of polycrystalline $Al_xTi_{1-x}N$ (x = 0, 0.25, 0.5, and 0.67) thin films under different substrate bias voltage (V_s) [21]. In this report, we examine the formation and evolution of biaxial stress, crystallographic texture, and grain size in $Al_{0.50}Ti_{0.50}N$ films deposited by varying substrate temperatures, while maintaining a constant substrate electrical bias of −40 V.

2. Experimental details

To deposit $Al_{0.50}Ti_{0.50}N$ films on the 100 surface of a 10 × 10 mm^2 Si substrate, a reactive cathodic arc evaporation technique was used. A 63 mm diameter $Al_{0.50}Ti_{0.50}$ metallic cathode (FK Grade, PLANSEE-Germany) was used at a fixed arc current of 75 Amperes. The angle formed by the surface normal of the cathode and the normal of the substrate was 35°. A substrate rotation speed of 5 rotations per minute was maintained. The details of the experimental setup was previously discussed [20,21]. The pure N_2 (99.9995%) pressure was kept constant at 40 mTorr during depositions. The substrate was heated using an 808 nm infrared laser diode-based heating unit. In this study, four different substrate temperatures (T_s) were used for thin film deposition: 250, 450, 600, and 750 °C. A DC power supply was used to electrically bias the substrate with a fixed voltage of −40 V.

In-situ 2-dimensional (2D) x-ray diffractograms (XRD) in grazing incident transmission mode were recorded at the P07 beamline at PETRA III (DESY, Germany). The grazing angle was fixed at 0.2° and the x-ray energy was 73.79 keV. A fixed beam slit widths of 100×600 μm^2 was used. A 2D flat panel detector with a 2048×2048-pixel resolution was used to record the diffractograms (PerkinElmer XRD 1622). One diffractogram requires 0.2 s of exposure time to record, and ten of which were superimposed to create the final diffractogram. The diffractogram of NIST standard LaB_6 powder was used to measure the distance between the substrate and the detector. The detector was placed to capture one quadrant of the diffraction pattern to maximize resolution. The 2D XRD were converted into 1D-line profiles using pyFAI [22], a Python-based program that integrates the intensities using 5° wide azimuthal bins (ΔΦ). To obtain the peak positions and peak widths of the diffraction peaks, the intensity vs. 2θ data was fitted with a pseudo-Voigt function. The biaxial stress was determined by the well-known $sin^2\psi$ method. The unstrained interplanar spacing (d^0_{hkl}) was determined from the d_{hkl} vs. $sin^2\psi$ plot and is corresponding to d_{hkl} value at the corresponding invariant tilt angle ψ^*, i.e., $d^0_{hkl} = d_{hkl}(\psi = \psi^*)$. The ψ^* was determined by the relation: $\sin^2\psi^* = \frac{2\nu_{hkl}}{1+\nu_{hkl}}$, here ν_{hkl} is the Poisson ratio for the *hkl* orientation of the films. In determination of biaxial stress, the 111 diffraction peak was used. High temperature elastic coefficients of FCC- $Al_{0.50}Ti_{0.50}N$ were used to estimate strain and stress from the work of Shulumba et al. [23] and are tabulated in Table 1.

The average crystallite size $\langle D_{hkl}\rangle$, which is averaged over the Debye-Scherrer rings, at a given instant during the deposition is estimated using Scherrer method [24] and is given by:

$$\langle D_{hkl}\rangle = \frac{1}{N(\Delta\Phi_i)} \sum_{\Delta\Phi_{i=1}}^{N} \frac{0{\cdot}9 \times \lambda}{\beta(\Delta\Phi_i) \times \cos\theta(\Delta\Phi_i)} \quad (1)$$

$N(\Delta\Phi_i)$ is the number of azimuthal bins. $\beta(\Delta\Phi_i)$ is the full width at half maximum of the pattern of individual intensity vs. 2θ plots for a given value of $\Delta\Phi_i$ and θ is the corresponding half of the scattering angle (2θ). λ is the wavelength of the x-ray beam and is 0.168 Å for this study.

The ex-situ characterization of the films is carried out by using scanning (SEM, Leo 1550 Gemini with an electron acceleration voltage of 4–5 kV), transmission (TEM) and scanning transmission (STEM) electron microscopies (both performed on a FEI Tecnai G2 microscope operated at 200 kV). STEM was combined with both high angle annular dark field (HAADF) and energy dispersive x-ray spectroscopy (EDS) detectors. Prior to analysis by (S)TEM suitable thin specimens were prepared by using a cross beam focussed ion beam (FIB)/SEM instrument (Zeiss EsB 1540) using the standard lift out approach. Mechanical properties of the films such as hardness, and elastic recovery are obtained with a nanoindenter equipped with Berkovich diamond tip. The maximum load of the nanoindentations is set to 10 mN so the indentation depth is less than 10 % of the total film thicknesses. The hardness values are quantified by the method proposed by Oliver and Pharr [25]. At least 30 indents are used to calculate the mean values of hardness and their standard deviation.

3. Results and discussion

3.1. Ex-situ electron micrograph and crystallographic texture

The fractured cross-section SEM images of the films are presented in Fig. 1, where a typical nano-columnar thin film morphology is seen for samples deposited at T_s = 250 °C, 450 °C, and 600 °C whereas the film deposited at T_s = 750 °C has a nanocrystalline like morphology (see-Fig. 1(d)). The $Al_{0.50}Ti_{0.50}N$ thin film deposited with T_s = 250 °C shows a

Table 1
Temperature dependent elastic coefficients of FCC- $Al_{0.50}Ti_{0.50}N$ used in determination of biaxial stress in thin films. The values are obtained from the work of Shulumba et al. [23].

T_s (°C)	C_{11} (GPa)	C_{12} (GPa)	C_{44} (GPa)	E_{111} (GPa)	ν_{111}	ψ^* (°)
250	410	134	178	422.9	0.188	32.52
450	394	130	171	406.67	0.189	32.59
600	382	127	166	394.9	0.189	32.63
750	369	123	161	382.79	0.1887	32.57

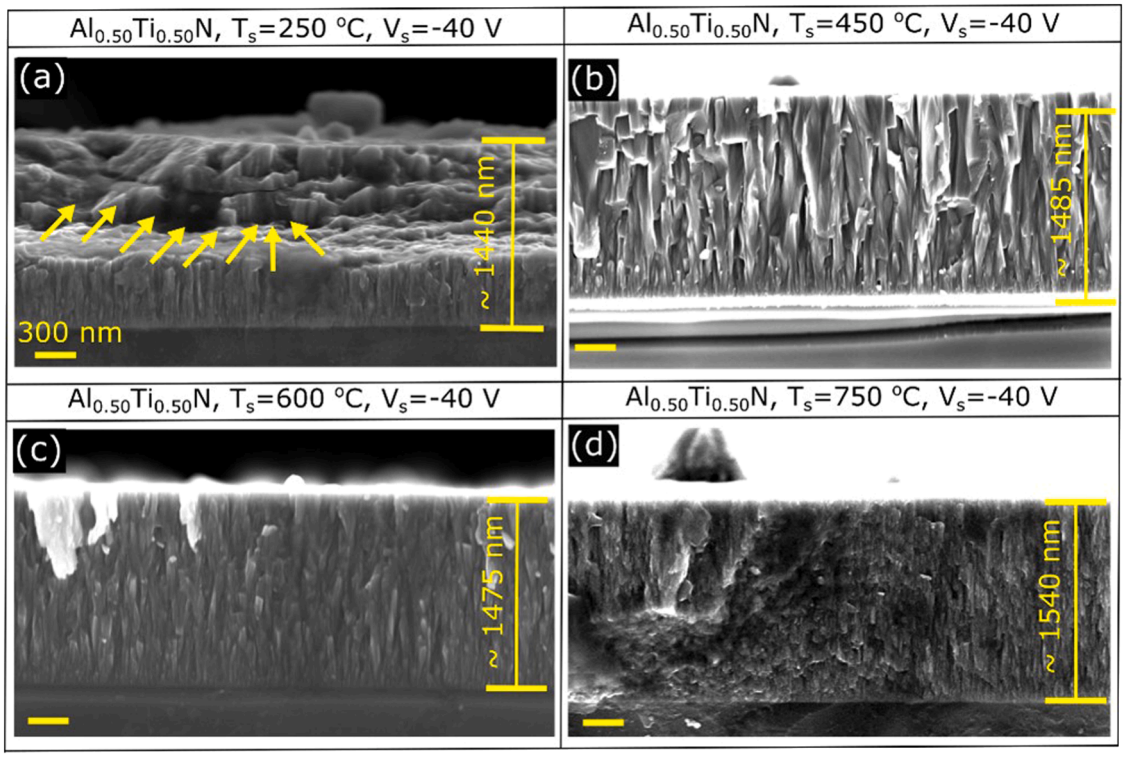

Fig. 1. shows the fractured cross-sectional FESEM images of $Al_{0.50}Ti_{0.50}N$ films deposited at substrate temperatures of 250 °C (a), 450 °C (b), 600 °C (c), and 750 °C (d). The yellow-coloured arrow-marked region in figure (a) shows a cohesive failure region in the film. (For interpretation of the references to colour in this figure legend, the reader is referred to the web version of this article.)

variation in film thickness across the film (Fig. 1(a)) indicating the cohesive failure of the film during its deposition. A plan view SEM inspection of the films confirms the delamination of the film from the substrate. From the visual inspection of the SEM images, the width of the nanocolumns is maximum for film deposited at T_s = 450 °C, and minimum for film deposited at T_s = 750 °C. The total film thickness t_f is highest (≈ 1540 nm) for films deposited at T_s=750 °C compared to other three films studied here.

Analysis of the 2D x-ray diffractograms from the films revealed that for all the T_s that are discussed here, the $Al_{0.50}Ti_{0.50}N$ films crystallized in an FCC structure (see Fig. 2). The diffraction from 111 crystal planes (c-111) of FCC-$Al_{0.50}Ti_{0.50}N$ appeared close to the 2θ of ≈ 3.9°−4.0° (i.e., the interplanar spacing d_{111} ≈ 2.42 Å), while diffraction from c-200 appeared at 2θ ≈ 4.5°−4.6° (d_{200} ≈ 2.12 Å). The diffraction signal at 2θ ≈ 6.4°−6.5° is from c-220 crystal planes, which correspond to d_{220} ≈ 1.49 Å. It can be clearly seen from Fig. 2 that in the films deposited with T_s = 250 °C, c-200 is textured along the GD, while c-111 is textured at Φ ≈ 35° (see Fig. 2(a)). Thus, the c-111 are 55° tilted away from the GD, in agreement with the crystallographic angle between c-200 and c-111 in FCC lattice (∼ 54.7°). With increase in T_s to 450 °C, the diffraction signal from c-111 is more randomly distributed in Φ, but three local intense regions are identified; (i) at Φ ≈ 33°, (ii) Φ ≈ 56°, and (iii) Φ ≈ 90° (see Fig. 2(b)). The c-200 crystal planes remain textured, but the angles at which the intense diffraction spots appear are at Φ ≈ 15° and at Φ ≈ 75° (see Fig. 2(b)). The $Al_{0.50}Ti_{0.50}N$ film deposited with T_s=600 °C shows a similar diffraction pattern as the coating grown at 450 °C. In this case, the three intense diffraction spots of c-111 appear at Φ ≈ 33°, 60°, and 90°. The intense spots on c-200 Debye-Scherrer ring are at Φ ≈ 18°, and 69° (see Fig. 2(c)). The diffraction pattern recorded for the $Al_{0.50}Ti_{0.50}N$ film deposited at T_s=750 °C differs from the others. Firstly, the diffraction intensity recorded from the sample is relatively low despite using the same geometry and x-ray flux. The diffraction pattern shows that both c-111 and c-200 are weakly textured. However, the most intense diffracted intensity is seen at Φ ≈ 54° for c-111 and Φ ≈ 47° for c-200.

To further validate our in-situ findings, we carried out ex-situ characterization with TEM of the films deposited at T_s = 450 °C and 750 °C, as shown in Fig. 3. Fig. 3(a1) is the bright field TEM micrograph of the film deposited at T_s = 450 °C which shows the formation of nanocolumns approximately 50–100 nm wide with no evidence of any voids or under-dense grain boundaries. For the first ≈ 300 nm of deposition, where a large number of narrower columns are seen (see Fig. 3(a1)), consistent with our previous observations [21] and with competitive grain growth. The SAED patterns were recorded at four different locations along the GD and marked as coloured circles in Fig. 3(a1). The SAED pattern recorded at the top of the film (see orange coloured circle in Fig. 3(a1) and (a3)) shows the formation of spotty diffraction patterns, indicating the formation of larger grain sizes with film growth. To verify that the diffraction pattern is representative of the film structure, we recorded SAED patterns from multiple locations on the top part of the film and found that all patterns were consistent. The intense diffraction spots corresponding to c-200 are slightly tilted away from the GD, agreeing well with our in-situ XRD data (see Fig. 2(b)). In this case, a combination of 111 and 113 crystal planes from FCC-$Al_{0.50}Ti_{0.50}N$ appear to be preferred along the GD. Similar observations are made from the SAED pattern recorded from the middle of the films (see Fig. 3(a4)). The SAED pattern recorded at the bottom of the film showed a range of preferential orientations centred on c-200 along the GD, indicating at the initial stage of the film's deposition its grains are small and c-200 oriented along the GD.

Fig. 3(b1) represents bright field TEM images of film deposited with T_s = 750 °C, which revealed a densely packed nanocrystalline-like morphology. The SAED patterns recorded at different film thickness (see coloured circle in Fig. 3(b1)) are presented as Fig. 3(b3-b6). Rather than having discrete spots, as for the film deposited at 450 °C, the patterns consist of defined arcs. This indicates that the film is composed of grains that are extremely small, 5–15 nm, and with preferred orientation different from the 450 °C case. It is quite clear that, irrespective of the

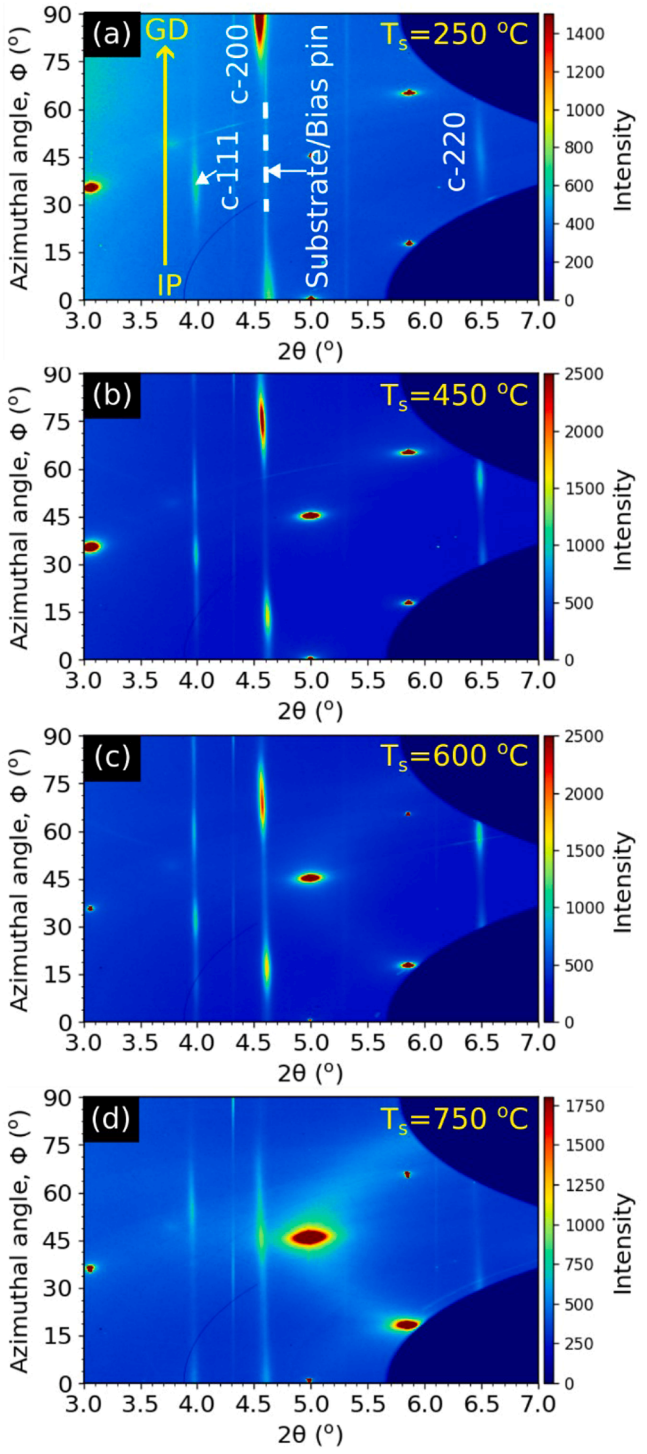

Fig. 2. shows the polar transformed 2D x-ray diffractograms of $Al_{0.50}Ti_{0.50}N$ films deposited at a substrate temperature of 250 °C (a), 450 °C (b), 600 °C (c), and 750 °C (d) at the end of their depositions. For Φ = 90° and 0°, the growth direction (GD) and in-plane (IP) directions are assigned.

film thickness, the c-220 crystal planes of FCC-(Al, Ti)N are predominantly textured along the GD, while c-111, and c-200 crystal planes textured close to 35–45° tilted away from the GD (see Fig. 3(b3-b6)), in agreement with our in-situ XRD findings (see Fig. 2(d)). It was also observed that diffractograms from both c-111 and c-200 planes appeared very close to each other in azimuthal angle, Φ. This suggests that there was some coherency between both c-111 and c-200 oriented grains in the film. Besides the diffraction pattern from FCC-(Al, Ti)N, we observed a faint diffraction pattern from 0002 crystal planes (h-0002) of hexagonal-closed-packed (HCP)-(Al, Ti)N (see the red coloured arrow marked in Fig. 3(b3-b6)). We also note that the diffraction from c-111 and h-0002 have the same azimuthal angle (Fig. 3(b3-b6)), suggesting that the c-111 and h-0002 crystal planes nucleate on top of each other. To further assess the effect of substrate temperature on fluctuations in elemental composition over film thickness, we recorded the STEM-EDS mapping of Si, Al, Ti, and N in both films, which are shown as Fig. 3(a2) and (b2) respectively. We did not observe any measurable compositional modulation in the films, and Al, Ti, and N form a uniform solid solution over the film thickness (see Fig. 3(a2) and (b2)).

3.2. *In-situ texture evolution*

Motivated by the ex-situ TEM and SAED data, we analysed the texture evolution of c-200 planes of (Al, Ti)N thin films deposited at different T_s (see Fig. 4). The film deposited at T_s = 250 °C shows that c-200 crystal planes are aligned along the GD (Φ=90°) throughout the film thickness, t_f (see Fig. 4(a)). Contrary to this, as mentioned previously, film deposited at T_s = 450 °C and 600 °C show that c-200 crystal planes are textured at a certain tilt angle to the GD. Interestingly, as the t_f increases, the tilt angle of the c-200 texture also increases. The change in tilt angle as the t_f increases from 300 nm to ~1450 nm is estimated to 7° and 10° for film deposited with T_s = 450 and 600 °C respectively (see (b-c)). The results agree well with the SAED pattern recorded from thin film deposited with T_s = 450 °C (see Fig. 4(a3-a6)). The c-200 of the film that was deposited at T_s = 750 °C have a texture that is relatively broad along Φ, but the intense spots only occur at Φ ≈ 45° and stay consistent throughout the thickness of the film (see Fig. 4(d)). Thus, two important observations are made from *ex-situ* data:

(i) In polycrystalline thin films of (Al,Ti)N, if c-200 crystal planes are tilted away from the GD, a mixed of c-111+c-113 textures develops along the GD.
(ii) There is a consistent increase in the tilt angle of c-200 planes of grains that are formed far from the interface of the films compared to towards the interface of the films.

The texture formation of c-200 crystal planes along the GD is well documented in the literature, and is often attributed to the minimization of surface energy, strain energy, and the channelling effect of ions at lower substrate bias voltages (e.g., −40 V) that are observed in films deposited at T_s = 250 °C. However, the microscopic origin of the off-axis tilt of 200 crystal planes away from the GD has been debated throughout the literature. Rafaja et al. [26] attribute the inclined preferred orientation in AlTiN deposited by arc evaporation to the geometry of the deposition system with a non-rotating substrate. Wahlström et al. [27] argued the tilted texture of magnetron sputtered AlTiN films is due to the oblique path between the substrate and magnetron targets. Je et al. [28] attributed the ±5° tilt of the 002 planes in TiN to competitive growth of 111 and 200 oriented grains, and to maintain the overall growth direction of 111 oriented grains close to the surface normal, the 200 oriented grains are tilted away. The inclined texture of nanostructured $Al_{1-x}Ti_xN$ is attributed to twin faults developed in the lattice by Kalss et al. [29]. Falub et al. [17] argued an interdependence of texture and stress in arc evaporated AlTiN thin films and suggested stress can influence the texture formation, and the tilt angle increases with an increase in the level of stress in the films. A similar interpretation is made for CrN [30–32] and $Ti_{0.67}Al_{0.33}N$ [33] thin films, where the transition of texture from c-200 to c-113 is attributed to a decrease in stress and film density. Karimi et al. [34] suggest that competitive growth promotes the formation of c-111-oriented grains, and to accommodate growth of this c-111-oriented grain, the c-200-oriented grains are tilted away from the GD. It was observed that with an increase in substrate temperature, the tilt angle of c-200 reduces owing to an increase in adatom mobility at higher substrate temperatures [34].

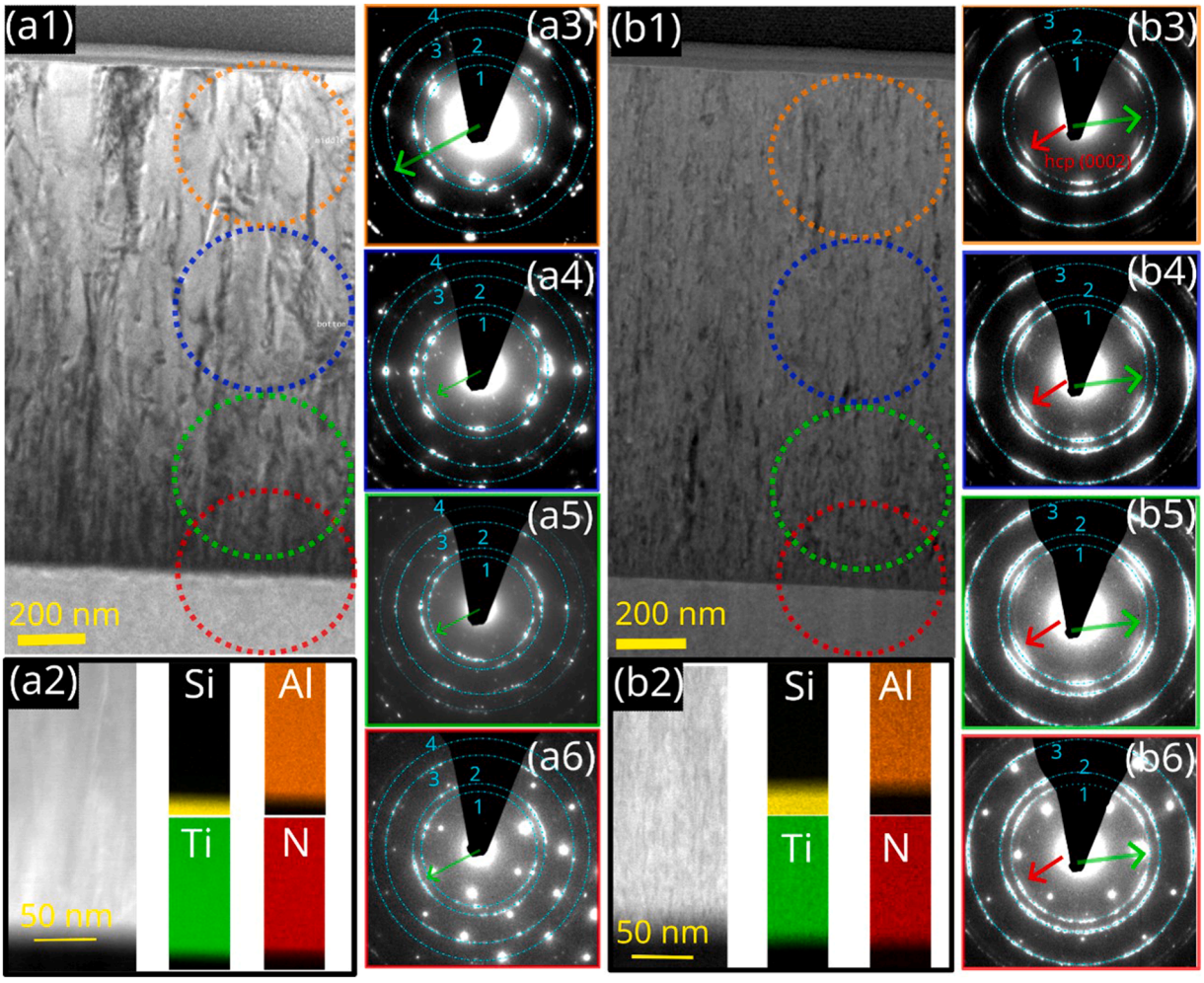

Fig. 3. shows the TEM analysis of the $Al_{0.50}Ti_{0.50}N$ thin films deposited with a substrate temperature, T_s, of 450 °C (a1-a6) and 750 °C (b1-b6). Figures a1, b1 are the TEM images; a2, b2 are STEM micrographs and EDS mapping of the elements, and a3-a6, b3-b6 are the SAED patterns recorded at various locations (shown as dotted-coloured circles at Figure a1) of the films deposited at T_s = 450 °C and 750 °C, respectively. The diffraction spots/pattern present on the circumference of circles marked as 1, 2, 3, and 4 on Figures a3-a6 and b3-b6 are identified as being from the 111, 200, 220, and 113 crystal planes of FCC-(Al, Ti)N. The green arrows in a3-a6 and b3-b6 represent the growth direction. The red arrows in Figures b3-b6 show diffraction from the 0002 planes of HCP-(Al,Ti)N. (For interpretation of the references to colour in this figure legend, the reader is referred to the web version of this article.)

In our study, the off-axis tilt of c-200 texture cannot be attributed to the oblique incidence of metal vapours toward the substrate, as previously argued [26,27,35], because perfect alignment of c-200 texture along the GD is observed with film deposited at the same geometrical configuration (i.e., 35° inclination angle), but at a relatively lower T_s of 250 °C. Our in-situ stress analysis (see Fig. 5(a-d)) revealed that the stress level in films is also not responsible for the tilt of the c-200 texture as proposed by Falub et al. [17] and Karimi et al. [33]. The $Al_{0.50}Ti_{0.50}N$ thin film deposited at T_s = 250 °C shows high stress state (see Fig. 5(a)), but the c-200 planes are perfectly textured along the GD. Between films deposited at T_s = 450 °C and 600 °C, the latter shows a lower stress (Fig. 5 (b-c)) and a higher off-axis tilt angle of c-200 than the former ones, contradicting the predictions by Falub et al. [17]. and Karimi et al. [33]. A consistent increase in tilt angle with an increase in substrate temperature is also in contradiction to the model proposed by Karimi et al. [33]. We propose that in these samples, along with the competitive growth mechanisms, other factors such as that which causes film surface roughening (e.g., the shadowing effect) during deposition [36] are together responsible for the off-axis tilt of c-200 in films deposited with T_s = 450 °C and 600 °C.

To the best of our knowledge, there is no report on the dynamics of texture evolution that are determined in real time during the film depositions. The literature has never documented a constant rise in off-axis tilt with film thickness except observations made by Kubec et al. [37] in a multi-layered TiN and SiO_x thin film and was attributed to the difference in nucleation nature between the substrate and SiO_x buffer layer and between two TiN layers.

The formation of c-220 texture, as seen in the film deposited with a T_s of 750 °C, in TMNs' thin films deposited with PVD and CVD is seen previously. Often in PVD deposition process, the c-220 textured was seen, when depositions were carried out with high energetics ions [38–40] as ⟨220⟩ direction has the high degree of channelling effect in FCC lattice. While in CVD-deposited thin films, the formation of c-220 texture is attributed to the formation of twinned crystallites at temperatures lower than 1200 °C [41], and the formation of twinned crystallites is attributed to the lower adatom mobility. To gain a microscopic insight into the c-220 texture formation in $Al_{0.50}Ti_{0.50}N$ film with T_s = 750 °C, we probed the atomic scale crystal using HR-TEM. As the c-220 textured from at the very initial stages of depositions (as seen from the SAED pattern, see Fig. 3(b6)) towards the interface of the film and substrate. Below a film thickness of 5 nm, the lattice planes could not be clearly resolved (see Fig. 6(a)). However, beyond that, the formation of specific crystalline grains is seen. The formed grains are found to be faceted (see the yellow dotted lines in Fig. 6(a) and the angle between

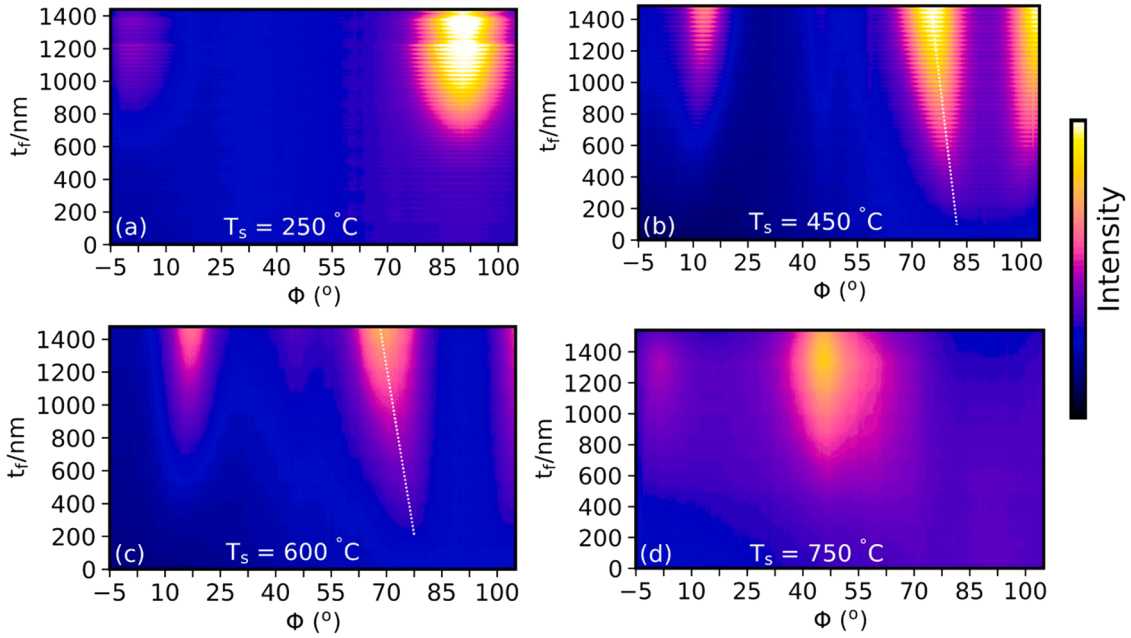

Fig. 4. shows the evolution of texture of 200 crystal planes of FCC-(Al,Ti)N along the azimuthal angle(Φ) for film deposited with a substrate temperature, T_s, of 250 °C (a), 450 °C (b), 600 °C (c), and 750 °C (d).The dotted lines in (b) and (c) are guided lines for change in Φ as t_f increases.

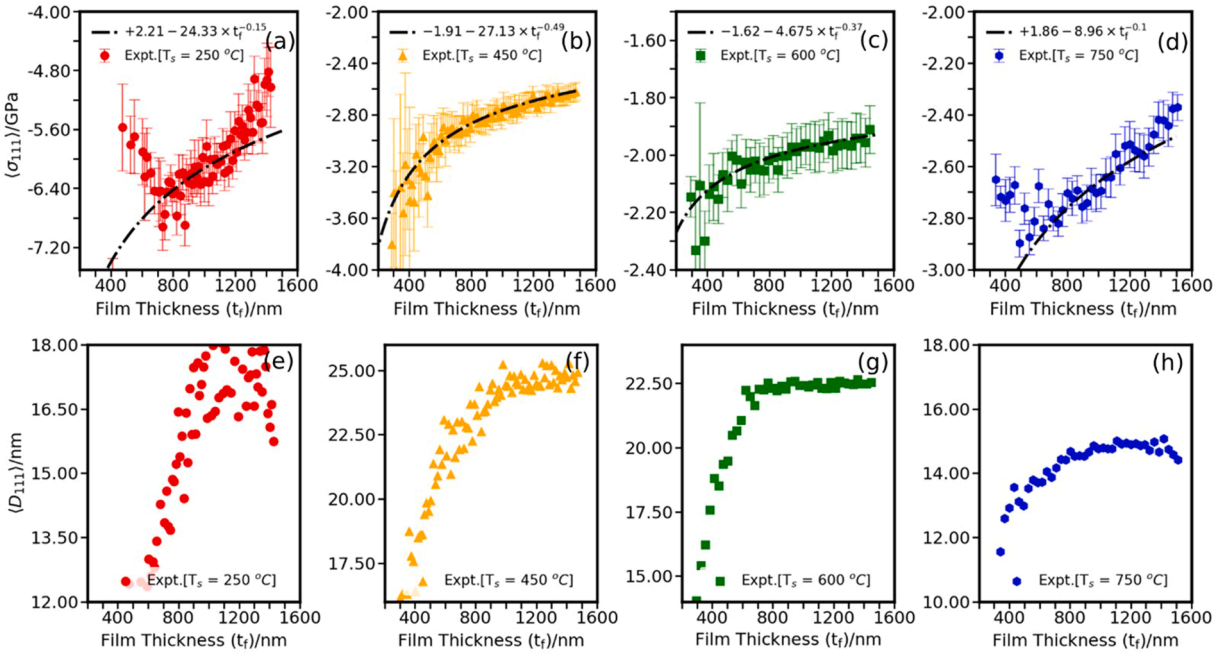

Fig. 5. (a-d) shows the evolution of biaxial stress $\langle\sigma_{111}\rangle$ as a function of film thickness, t_f, of $Al_{0.50}Ti_{0.50}N$ at a substrate temperature of 250 °C, 450 °C, 600 °C and 750 °C respectively. Figure (e-h) shows the temporal evolution of the average crystallite size $\langle D_{111}\rangle$ of the films deposited at a substrate temperature of 250 °C, 450 °C, 600 °C, and 750 °C, respectively.

the normal of the crystal facets and the normal of the film/substrate interface varies from 35° to 45°. The FFT pattern (see Fig. 6(b)) also showed that the strongest intensity of the c-111 lattice planes was tilted away from the GD, along with a lower intensity of both c-111 and c-200 crystal planes being aligned along the GD. This established formation of c-111 crystal facets at very initial stages of depositions ($t_f \approx$15 nm) starts. A similar analysis for the film deposited with T_s= 450 °C showed an intense texture of c-200 along the GD. The formation of these crystal facets could be driven by the change in supersaturation of Al in $Al_{0.50}Ti_{0.50}N$ at this high temperature (T_s = 750 °C) [42]. These newly formed facets are responsible for the further nucleation of tilted, 111-oriented grains. And since the angle between c-111 and c-220 crystal planes in the FCC lattice is 35.3°, the c-220 planes are textured along the GD in this case. The frequent re-nucleation induced nano-crystalline surface morphology, relatively higher growth rate, and formation of minute HCP-$Al_xTi_{1-x}N$ in this film suggest the film is grown under high supersaturation [43,44]. The appearance of the diffraction pattern of h-0002 crystal planes of HCP-$Al_xTi_{1-x}N$ and c-111 of FCC-$Al_{0.50}Ti_{0.50}N$ along the same azimuthal angle (as seen in Fig. 3 (b3-b6)) is commensurate with the symmetry and low lattice mismatch

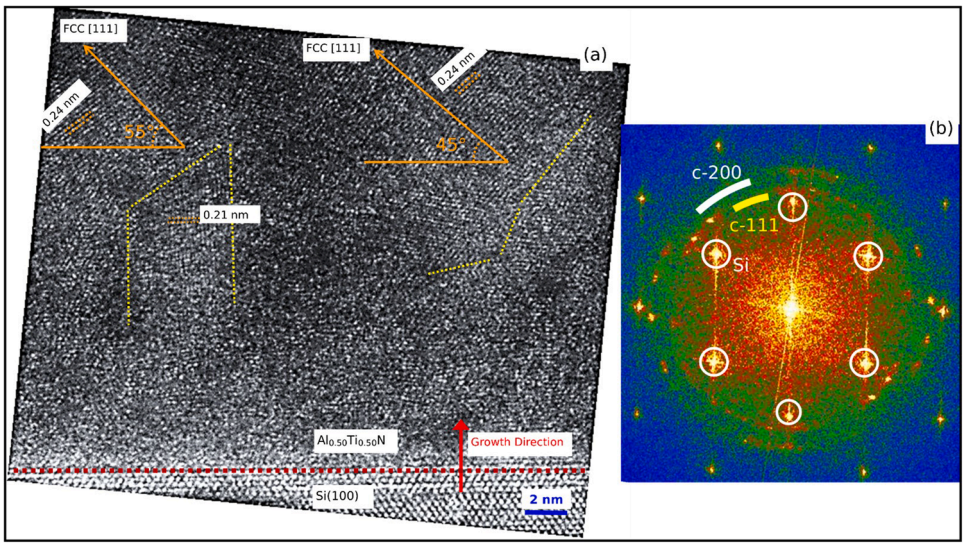

Fig. 6. is the HRTEM image (a) and Fast Fourier Transformation (FFT) pattern (b) of the interface region of the $Al_{0.50}Ti_{0.50}N$ thin film grown on Si (100) substrate deposited at $T_s = 750$ °C.

between these planes [45].

3.3. In-situ stress and average grain size evolution

The evolution of biaxial stress $\langle\sigma_{111}\rangle$ with t_f of $Al_{0.50}Ti_{0.50}N$ films deposited with various T_s is presented in Fig. 5(a-d). We find that because the diffracted intensities are modest, it is challenging to quantify the $\langle\sigma_{111}\rangle$ until after the film thickness, t_f, approaches 300 nm. For the film deposited with $T_s = 250$ °C the compressive $\langle\sigma_{111}\rangle$ increases consistently between $t_f \approx 800$ nm and $t_f \approx 400$ nm, it changes from −5.6 ± 0.7 GPa to −6.4 ± 0.3 GPa (see Fig. 5(a)), but at higher t_f the $\langle\sigma_{111}\rangle$ decreases as t_f increases (see Fig. 5(a)) suggesting a compressive stress relaxation with film thickness. The film deposited at $T_s = 450$ °C shows a clear power-law like relaxation of $\langle\sigma_{111}\rangle$ with t_f (see Fig. 5(b)). The power law fitting ($\sigma = \sigma_0 + c \times t_f^{-\gamma}$) reveals that the σ_0, c, and γ to be −1.91 GPa, −27.13 GPa nm^{γ}, and 0.49 respectively. A similar power-law-like evolution of $\langle\sigma_{111}\rangle$ with t_f is also seen in film deposited at $T_s = 600$ °C, except for the fact that σ_0, c, and γ are −1.62 GPa, −4.675 GPa nm^{γ} and 0.37 respectively (see Fig. 5(c)). The evolution of $\langle\sigma_{111}\rangle$ with t_f for the film deposited with $T_s = 750$ °C is different than the previously discussed ones. Between $t_f \approx 300$ nm and $t_f \approx 750$ nm the $\langle\sigma_{111}\rangle$ increases, while at larger t_f a consistent relaxation of $\langle\sigma_{111}\rangle$ is observed (see Fig. 5(d)). Fitting of the power-law within the t_f between 750 nm to 1540 nm suggests σ_0, c, and γ are +1.86 GPa, −8.96 GPa nm^{γ}, and 0.10 respectively (see Fig. 5(d)).

Further, we monitored the evolution of average grain/domain size $\langle D_{hkl}\rangle$ over a film thickness t_f, shown in Fig. 5 (e-h). The film deposited with $T_s = 250$ °C shows a consistent increase in $\langle D_{111}\rangle$ from 12.5 nm to 18.2 nm as t_f increases from 400 nm to 1250 nm, beyond which a scattered value of $\langle D_{111}\rangle$ is seen (see Fig. 5(e)). When T_s is raised to 450 °C, the estimated $\langle D_{111}\rangle$ increases from 16.3 nm to 25.2 nm, as t_f increases from 300 nm to 1485 nm (see Fig. 5(f)). When the T_s is set to 600 °C, the evolution of $\langle D_{111}\rangle$ changes and it increases from 14.1 nm to 22.2 nm as t_f increases from 300 nm to 620 nm, beyond which it remains approximately constant (see Fig. 5(g)). At high T_s of 750 °C, the change in $\langle D_{111}\rangle$ is very small, and it increases from 11.5 nm to a maximum of 14.6 nm, as t_f increases from 300 nm to 1540 nm (see Fig. 5(h)).

3.4. Correlation of internal stress and grain size: identification of critical grain size D_0

The generation of compressive stress in polycrystalline thin films is widely reported in the literature and is attributed to densification of grain boundaries and the generation of defects in the bulk by high energetics ions [46,47]. The generation of compressive stress in our films agrees with the literature, as the films are deposited with a −40 V of substrate bias. However, the stress relaxation associated with an increase in total film thickness, t_f, needs to be explained. Also, the microscopic origin of anomalies in the $\langle\sigma_{111}\rangle$ evolution in films deposited at $T_s = 250$ °C and 750 °C needs to be examined. The relaxation of compressive stress in films with an increase in film thickness indicates that a tensile component is being generated, often due to grain growth or larger average domain sizes. The contribution from the tensile component of grain growth and the compressive component due to grain boundaries and adatom attachment to 2D islands formed at the surfaces of grains, were deconvoluted by Thompson et al. [48]. The instantaneous tensile stress due to grain growth (σ_{in}^{gg}) is given by;

$$\sigma_{in}^{gg}(d) = \frac{E}{1-\nu}\frac{\Delta a}{d}\left(\frac{1}{1+\left(\frac{E}{1-\nu}\right)\frac{\Delta a}{d}\frac{1}{\sigma_y}}\right) \quad (2)$$

where E, and ν are Young's modulus and Poisson's ratio, respectively. The d, Δa, and σ_y represent the average grain size, excess free volume associated with grain boundaries, and biaxial tensile stress yield limit, respectively. The authors [48] further argued that the instantaneous stress generated by the newly deposited surface layer ($\sigma^*(t)$) is the ratio of the capture probability of adatoms to the grain boundary ($N_{adatoms\text{-}GB}$) and to the newly formed 2D islands ($N_{adatoms\text{-}2Disland}$). Thus, the compressive component of instantaneous stress is;

$$\sigma_{in}^{comp} = -\frac{E}{1-\nu}\frac{2p\delta}{d} \quad (3)$$

where p is the capture probability of the adatoms by the grain boundary, and δ is the average distance between the 2D islands and the grain boundaries. In the smaller grain limit of $d < L_{island}$, L_{island} being the 2D island spacing, the σ_{in}^{comp} is independent of grain size, d. The transition of σ_{in}^{comp} being independent of d to its inverse dependence to d occurs at $d = L_{island}$. We checked, if above discussed mechanism is being dominated in

determination of the $\langle\sigma_{111}\rangle$, and if that explains the increase in $\langle\sigma_{111}\rangle$ with increase in t_f in films deposited with $T_s = 250$ °C and 750 °C (see Fig. 5(a) and (d)). We evaluate the instantaneous compressive stress σ_{in}^{comp} (= $\langle\sigma_{111}\rangle$-$\sigma_{in}^{gg}(d)$) for all four films. In evaluation of $\sigma_{in}^{gg}(d)$ (mentioned as σ_{111}^{gg} in Fig. 7), we used $\Delta a = 1$ Å, and σ_y to 830 MPa (the maximum converged tensile stress recorded from a similar study [21]) in Eq. (2). The instantaneous d is approximated to $\langle D_{111}\rangle$. For E and ν, the high temperature values of E_{111} and ν_{111} were used.

The estimated σ_{in}^{comp} vs $\frac{1}{d}$ (or $\frac{1}{\langle D_{111}\rangle}$) is shown in Fig. 7. Clearly two regimes of scaling of stress with $\frac{1}{\langle D_{111}\rangle}$, with $\frac{1}{\langle D_{111}\rangle} = 0.072\ \text{nm}^{-1}$ being the boundary line, is seen. When $\frac{1}{\langle D_{111}\rangle}$ is less than 0.072 nm^{-1}, there is a linear dependence of σ_{in}^{comp} to $\frac{1}{\langle D_{111}\rangle}$, whereas for larger values of $\frac{1}{\langle D_{111}\rangle}$, σ_{in}^{comp} is independent of $\frac{1}{\langle D_{111}\rangle}$. Thompson et al. [48] proposed that the transition from inverse dependence to independence of σ_{in}^{comp} occurs at $d = L_{island}$. Thus, we identify the L_{island} to $1/0.072\ \text{nm}^{-1} = 13.9$ nm. We also estimated $\sigma_{in}^{gg}(d)$ by varying Δa from 0.5 Å to 1 Å and σ_y from 500 MPa to 1.0 GPa and analysed the depencence of σ_{in}^{comp} to $\frac{1}{\langle D_{111}\rangle}$. The obtained results are similar as discussed above. As a result, we suggest that, for grain sizes smaller than 13.9 nm, the compressive stress, $\langle\sigma_{111}\rangle$, does not relax with increasing film thickness, despite an increase in grain size with increasing film thickness. In this grain size regime, the capture probability of adatoms at the grain boundary is higher than that of the 2D islands formed on top of grains, leading to the generation of compressive stress. With grain size larger than 13.8 nm, the effect is reversed, and the capture probability of adatoms on 2D islands increases as grain size increases, leading to a reduction in the magnitude of compressive stress and hence a small stress relaxation observed in our films. The calculated L_{island} is in close agreement with our earlier predictions of the mean grain size ($D_0 = 13.4 \pm 3.6$ nm) at which discrete islands shift to continuous films in $Al_xTi_{1-x}N$ coatings [21]. The computed L_{island} and D_0 are within the range of 2D island spacing anticipated by classical nucleation theory [49].

The relatively smaller grain size in film deposited at $T_s = 250$ and 750 °C compared to $T_s = 450$ and 600 °C can be understood as follows:

(i) Because of the lower substrate temperature, T_s, the adatom mobility as well as the grain boundary mobility are smaller, and hence the grain growth rate is lower. This leads to a smaller grain size and, consequently, relatively narrow nanocolumns and an intercolumnar gap (as seen in Fig. 1(a)).

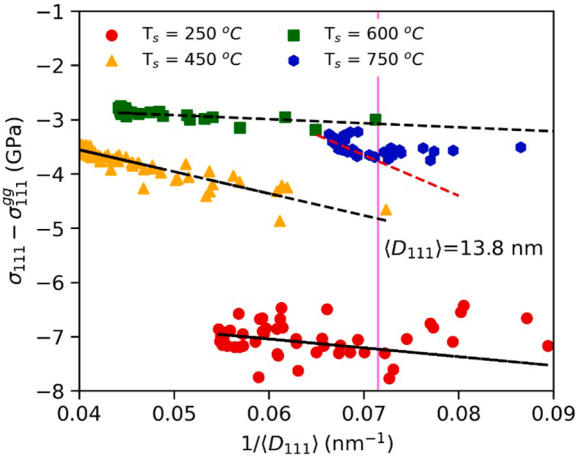

Fig. 7. shows instantaneous compressive stress ($\sigma_{in}^{comp} = \sigma_{in} - \sigma_{in}^{gg}(d)$) as a function of inverse of grain size ($\langle D_{111}\rangle$). Instantaneous stress σ_{in} was equivalent to σ_{111}. In estimation of $\sigma_{in}^{gg}(d)$ using Eq. (2), $\Delta a = 1.0$ Å and $\sigma_y = 830$ MPa is used. The dashed/solid lines over experimental scatter data points shows linear fitting of the experimental σ_{in}^{comp} vs inverse of $\langle D_{111}\rangle$.

(ii) Adatom mobility and grain boundary mobility both rise as the substrate temperature rises to 450 and 600 °C, causing grain growth and the emergence of wider and denser nanocolumns (as seen in Fig. 1(b-c) and Fig. 3(a1)).

(iii) At $T_s = 750$ °C, the development of smaller grain is a complex phenomenon. The formation of nanocrystalline microstructure hints that during thin film growth, grain nucleation occurs frequently. It is possible that the formation of hexagonal $Al_xTi_{1-x}N$ at grain boundaries, as previously observed, is what limits grain growth, as suggested by the occurrence of a faint diffraction from HCP-$Al_xTi_{1-x}N$ 0002 planes.

As previously mentioned, the $\langle\sigma_{111}\rangle$ evolution deviates from power-law after a total film thickness, t_f, of 1250 nm, and the scattered $\langle D_{111}\rangle$ does too in $Al_{0.50}Ti_{0.50}N$ thin films deposited at $T_s = 250$ °C (see Fig. 5(a) and (e)). We also observe a discontinuity at the same t_f in the evolution of the integrated intensity of diffraction patterns from crystal planes c-111 and c-200. The SEM also demonstrates the film's lack of coherence (see Fig. 1(a)). Our earlier work made a similar set of observations, which we attribute to cohesive failure of films due to high stress fields. The critical stress ($\sigma_{cr.}$) and critical film thickness ($h_{cr.}$) values, which correspond to the point(s) of discontinuity in the graph of $\langle\sigma_{111}\rangle$ vs t_f, can be used to calculate the plain strain fracture toughness (K_{IC}) [21,50,51]. The K_{IC} is estimated to be 4.45 ± 0.4 MPa.$m^{1/2}$ for an approximate $\sigma_{cr.} = \sigma_{111}$(at $t_f = 1250$ nm) and $h_{cr.} = 1250$ nm. This estimate is very similar to the $Al_{0.50}Ti_{0.50}N$ films deposited at a relatively higher bias voltage (−80 V), but it is slightly higher than previously reported values for $Al_{0.60}Ti_{0.40}N$ [1] and $Al_{0.46}Ti_{0.54}$ [52].

To characterize the effect of different microstructures to the mechanical properties of $Al_{0.50}Ti_{0.50}N$ films, we measured the mechanical hardness and elastic recovery from thin films deposited with $T_s = 450$, 600, and 750 °C. The recorded hardness values are 30.4 ± 1.4, 32.7 ± 0.9, and 30.9 ± 1.4 GPa. The elastic recovery is measured with a load of 10 mN and is found to be 43.7 %, 47.6 %, and 43.8 % for film deposited at $T_s = 450$, 600, and 750 °C, respectively. As the uncertainty in the estimation of hardness is larger than the difference in mean values, a definitive conclusion on the effect of microstructures on the mechanical hardness of $Al_{0.50}Ti_{0.50}N$ thin film deposited with cathodic arc evaporation could not be drawn conclusively.

4. Summary

We used in-situ 2D synchrotron x-ray diffraction to investigate the impact of substrate temperature on the in-situ internal stress, crystallographic texture, and grain/crystallite sizes of $Al_{0.50}Ti_{0.50}N$ thin films deposited on 100 surface of silicon using the reactive cathodic arc evaporation method. The thin films exhibited a single-phase FCC crystal structure and a nanocolumnar morphology, when they were formed at a substrate temperature of less than 600 °C. Small amounts of HCP phased $Al_xTi_{1-x}N$ formed at substrate temperature of 750 °C, along with the dominating FCC phase, resulting in a nanocrystalline-like morphology. We discovered that the temperature of the substrate has a significant influence on the development of crystallographic textures. The 200 crystal planes are oriented parallel to the film-substrate interface at low substrate temperature (250 °C). The 200 crystal planes are tilted away from the direction perpendicular to the normal of the film/substrate interface as the substrate temperature rises to 450–600 °C, and a combination of 111 and 113 crystallographic texture is generated along the growth direction. When the substrate temperature reaches 750 °C, a 220 crystallographic texture begins to form. We also see that the off-axis tilt of 200 crystal planes increases between 7°−10° as the film thickness increases from ~250 nm to ~1400 nm. In conjunction with an increase in average grain size with an increase in overall film thickness, we observe a power-law-like behaviour of biaxial stress relaxation with increasing film thickness for films grown at 450–600 °C. Our investigation showed that the biaxial compressive stress is independent of grain

size up to a certain size (determined as 14 nm for $Al_{0.50}Ti_{0.50}N$), after which the stress level scales with the inverse of average grain sizes. The highest degree of biaxial compressive stress, which leads to film cohesive failure, is seen in the thin film of $Al_{0.50}Ti_{0.50}N$ formed at a substrate temperature of 250 °C. The plain strain fracture toughness of $Al_{0.50}Ti_{0.50}N$ is estimated to be 4.45 ± 0.4 MPa.$m^{1/2}$, which is in good agreement with our earlier estimates.

CRediT authorship contribution statement

Sanjay Nayak: Conceptualization, Data curation, Formal analysis, Investigation, Methodology, Software, Visualization, Writing – original draft, Writing – review & editing. **Tun-Wei Hsu:** Writing – original draft, Writing – review & editing, Formal analysis, Methodology, Resources. **Robert Boyd:** Data curation, Investigation, Methodology, Resources, Visualization, Writing – original draft, Writing – review & editing. **Jens Gibmeier:** Supervision, Validation, Writing – original draft, Writing – review & editing, Funding acquisition, Investigation, Methodology, Project administration, Resources. **Norbert Schell:** Investigation, Methodology, Resources, Validation, Writing – original draft, Writing – review & editing. **Jens Birch:** Conceptualization, Funding acquisition, Methodology, Project administration, Resources, Supervision, Validation, Writing – original draft. **Lina Rogström:** Funding acquisition, Methodology, Project administration, Validation, Writing – original draft, Writing – review & editing. **Magnus Odén:** Funding acquisition, Methodology, Project administration, Resources, Supervision, Validation, Writing – original draft, Writing – review & editing.

Declaration of competing interest

The authors declare that they have no known competing financial interests or personal relationships that could have appeared to influence the work reported in this paper.

Acknowledgments

The synchrotron experiments were conducted at DESY under the proposal I-20210060EC. We acknowledge the financial support from the Swedish Research Council (grant no 2017-06701) via the Röntgen Ångström Cluster (RÅC) Frame Program, the competence center FunMat-II supported by Vinnova (grant no 2022-03071), and the Swedish government strategic research area grant AFM (SFO Mat LiU, grant no 2009-00971)

References

[1] M. Bartosik, C. Rumeau, R. Hahn, Z.L. Zhang, P.H. Mayrhofer, Fracture toughness and structural evolution in the TiAlN system upon annealing, Sci. Rep. 7 (2017) 16476.
[2] N. Norrby, M.P. Johansson, R. M'Saoubi, M. Odén, Pressure and temperature effects on the decomposition of arc evaporated Ti0.6Al0.4N coatings in continuous turning, Surf. Coat. Technol. 209 (2012) 203–207, https://doi.org/10.1016/j.surfcoat.2012.08.068.
[3] L. Hultman, G. Håkansson, U. Wahlström, J.E. Sundgren, I. Petrov, F. Adibi, J. E. Greene, Transmission electron microscopy studies of microstructural evolution, defect structure, and phase transitions in polycrystalline and epitaxial Ti1-xAlxN and TiN films grown by reactive magnetron sputter deposition, Thin Solid Films 205 (1991) 153–164, https://doi.org/10.1016/0040-6090(91)90297-B.
[4] G. Skordaris, K.D. Bouzakis, T. Kotsanis, P. Charalampous, E. Bouzakis, B. Breidenstein, B. Bergmann, B. Denkena, Effect of PVD film's residual stresses on their mechanical properties, brittleness, adhesion and cutting performance of coated tools, CIRP J. Manuf. Sci. Technol. 18 (2017) 145–151, https://doi.org/10.1016/j.cirpj.2016.11.003.
[5] M. Abdoos, B. Bose, S. Rawal, A.F.M. Arif, S.C. Veldhuis, The influence of residual stress on the properties and performance of thick TiAlN multilayer coating during dry turning of compacted graphite iron, Wear 454–455 (2020) 203342, https://doi.org/10.1016/j.wear.2020.203342.
[6] N. Schalk, C. Mitterer, J. Keckes, M. Penoy, C. Michotte, Influence of residual stresses and grain size on the spinodal decomposition of metastable Ti1-xAlxN coatings, Surf. Coat. Technol. 209 (2012) 190–196, https://doi.org/10.1016/j.surfcoat.2012.08.052.
[7] C. Wüstefeld, D. Rafaja, V. Klemm, C. Michotte, M. Kathrein, Effect of the aluminium content and the bias voltage on the microstructure formation in Ti1-xAlxN protective coatings grown by cathodic arc evaporation, Surf. Coat. Technol. 205 (2010) 1345–1349, https://doi.org/10.1016/j.surfcoat.2010.07.057.
[8] F. Lomello, F. Sanchette, F. Schuster, M. Tabarant, A. Billard, Influence of bias voltage on properties of AlCrN coatings prepared by cathodic arc deposition, Surf. Coat. Technol. 224 (2013) 77–81, https://doi.org/10.1016/j.surfcoat.2013.02.051.
[9] P. Patsalas, C. Charitidis, S. Logothetidis, The effect of substrate temperature and biasing on the mechanical properties and structure of sputtered titanium nitride thin films, Surf. Coat. Technol. 125 (2000) 335–340. www.elsevier.nl/locate/surfcoat.
[10] J. Bujak, J. Walkowicz, J. Kusiński, Influence of the nitrogen pressure on the structure and properties of (Ti,Al)N coatings deposited by cathodic vacuum arc PVD process, Surf. Coat. Technol 180–181 (2004) 150–157, https://doi.org/10.1016/j.surfcoat.2003.10.058.
[11] K.M. Calamba, J. Salamania, M.P.J. Jõesaar, L.J.S. Johnson, R. Boyd, J.F. Pierson, M.A. Sortica, D. Primetzhofer, M. Odén, Effect of nitrogen vacancies on the growth, dislocation structure, and decomposition of single crystal epitaxial (Ti1-xAlx)Ny thin films, Acta Mater. 203 (2021) 116509, https://doi.org/10.1016/j.actamat.2020.116509.
[12] R. Wuhrer, W.Y. Yeung, A comparative study of magnetron co-sputtered nanocrystalline titanium aluminium and chromium aluminium nitride coatings, Scr. Mater. 50 (2004) 1461–1466, https://doi.org/10.1016/j.scriptamat.2004.03.007.
[13] B.Y. Shew, J.L. Huang, The effects of nitrogen flow on reactively sputtered TiAlN films, Surf. Coat. Technol. 71 (1995) 30–36, https://doi.org/10.1016/0257-8972(94)02300-F.
[14] L. Combadiere, J. Machet, Reactive magnetron sputtering deposition of TiN films. I. Influence of the substrate temperature on structure, composition and morphology of the films Laurette, Surf. Coat. Technol. 88 (1996) 17–27.
[15] L. Combadiere, J. Machet, Reactive magnetron sputtering deposition of TIN films. II. Influence of substrate temperature on the mechanical properties of the films, Surf. Coat. Technol. 88 (1997) 28–37, https://doi.org/10.1016/S0257-8972(96)02870-8.
[16] Y.K. Wang, X.Y. Cheng, W.M. Wang, X.H. Gu, L.F. Xia, T.C. Lei, W.H. Liu, Microstructure and properties of (Ti, Al) N coating on high speed steel, Surf. Coat. Technol. 72 (1995) 71–77, https://doi.org/10.1016/0257-8972(94)02331-J.
[17] C.V. Falub, A. Karimi, M. Ante, W. Kalss, Interdependence between stress and texture in arc evaporated Ti–Al–N thin films, Surf. Coat. Technol. 201 (2007) 5891–5898.
[18] M. Beckers, N. Schell, R.M.S. Martins, A. Mücklich, W. Möller, The influence of the growth rate on the preferred orientation of magnetron-sputtered Ti-Al-N thin films studied by in situ x-ray diffraction, J. Appl. Phys. 98 (2005), https://doi.org/10.1063/1.1999829.
[19] J.E. Greene, J.-E. Sundgren, L. Hultman, I. Petrov, D.B. Bergstrom, Development of preferred orientation in polycrystalline TiN layers grown by ultrahigh vacuum reactive magnetron sputtering, Appl. Phys. Lett. 67 (1995) 2928–2930.
[20] J.L. Schroeder, W. Thomson, B. Howard, N. Schell, L. Näslund, L. Rogström, M. P. Johansson-Jõesaar, N. Ghafoor, M. Odén, E. Nothnage, A. Shepard, J. Greer, J. Birch, Industry-relevant magnetron sputtering and cathodic arc ultra-high vacuum deposition system for in situ x-ray diffraction studies of thin film growth using high energy synchrotron radiation, Rev. Sci. Instrum. 86 (2015) 95113.
[21] S. Nayak, T.-W. Hsu, L. Rogström, M. Moreno, J.M. Andersson, M.P. Johansson-Jõesaar, R. Boyd, N. Schell, J. Gibmeier, J. Birch, M. Odén, In-situ real-time evolution of intrinsic stresses and microstructure during growth of cathodic arc deposited (Al,Ti)N coatings (2022). https://arxiv.org/abs/2301.03935 Unpublished.
[22] J. Kieffer, V. Valls, N. Blanc, C. Hennig, New tools for calibrating diffraction setups, J. Synchrotron Radiat. 27 (2020) 558–566, https://doi.org/10.1107/S1600577520000776.
[23] N. Shulumba, O. Hellman, L. Rogström, Z. Raza, F. Tasnádi, I.A. Abrikosov, M. Odén, Temperature-dependent elastic properties of Ti1- x Al x N alloys, Appl. Phys. Lett. 107 (2015) 231901.
[24] A.L. Patterson, The Scherrer formula for X-ray particle size determination, Phys. Rev. 56 (1939) 978.
[25] W.C. Oliver, G.M. Pharr, Measurement of hardness and elastic modulus by instrumented indentation: advances in understanding and refinements to methodology, J. Mater. Res. 19 (2004) 3–20, https://doi.org/10.1557/jmr.2004.19.1.3.
[26] D. Rafaja, M. Šíma, V. Klemm, G. Schreiber, D. Heger, L. Havela, R. Kužel, X-ray diffraction on nanocrystalline Ti1- xAlxN thin films, J. Alloys Compd. 378 (2004) 107–111.
[27] U. Wahlström, L. Hultman, J.E. Sundgren, F. Adibi, I. Petrov, J.E. Greene, Crystal growth and microstructure of polycrystalline Ti1-xAlxN alloy films deposited by ultra-high-vacuum dual-target magnetron sputtering, Thin Solid Films 235 (1993) 62–70, https://doi.org/10.1016/0040-6090(93)90244-J.
[28] J.H. Je, D.Y. Noh, H.K. Kim, K.S. Liang, Preferred orientation of TiN films studied by a real time synchrotron x-ray scattering, J. Appl. Phys. 81 (1997) 6126–6133, https://doi.org/10.1063/1.364394.
[29] A. Karimi, W. Kalss, Off-axis texture in nanostructured Ti1 - xAlxN thin films, Surf. Coat. Technol. 202 (2008) 2241–2246, https://doi.org/10.1016/j.surfcoat.2007.08.074.
[30] L. Chekour, C. Nouveau, A. Chala, C. Labidi, N. Rouag, M.A. Djouadi, Growth mechanism for chromium nitride films deposited by magnetron and triode

sputtering methods, Surf. Coat. Technol. 200 (2005) 241–244, https://doi.org/10.1016/j.surfcoat.2005.02.062.
[31] M.A. Djouadi, C. Nouveau, O. Banakh, R. Sanjinés, F. Lévy, G. Nouet, Stress profiles and thermal stability of CrxNy films deposited by magnetron sputtering, Surf. Coat. Technol. 151–152 (2002) 510–514, https://doi.org/10.1016/S0257-8972(01)01635-8.
[32] C. Nouveau, M.A. Djouadi, M.A. Djouadi, O. Banakh, R. Sanjinés, F. Lévy, Stress and structure profiles for chromium nitride coatings deposited by r.f. magnetron sputtering, Thin Solid Films 398 (2001) 490–495, https://doi.org/10.1016/S0040-6090(01)01435-3.
[33] A.R. Shetty, A. Karimi, Formation of (113) texture in fcc nitride thin films and its influence on the film properties, Thin Solid Films 528 (2013) 255–262, https://doi.org/10.1016/j.tsf.2012.08.062.
[34] A.R. Shetty, A. Karimi, Texture change through film thickness and off-axis accommodation of (0 0 2) planes, Appl. Surf. Sci. 258 (2011) 1630–1638, https://doi.org/10.1016/j.apsusc.2011.10.037.
[35] Y.H. Sohn, R.R. Biederman, R.D. Sisson, Microstructural development in physical vapour-deposited partially stabilized zirconia thermal barrier coatings, Thin Solid Films 250 (1994) 1–7, https://doi.org/10.1016/0040-6090(94)90155-4.
[36] Y. Zhao, Y. Qian, W. Yu, Z. Chen, Surface roughness of alumina films deposited by reactive r.f. sputtering, Thin Solid Films 286 (1996) 45–48, https://doi.org/10.1016/S0040-6090(95)08514-9.
[37] J. Keckes, R. Daniel, J. Todt, J. Zalesak, B. Sartory, S. Braun, J. Gluch, M. Rosenthal, M. Burghammer, C. Mitterer, S. Niese, A. Kubec, 30nm X-ray focusing correlates oscillatory stress, texture and structural defect gradients across multilayered TiN-SiOx thin film, Acta Mater. 144 (2018) 862–873, https://doi.org/10.1016/j.actamat.2017.11.049.
[38] Y.H. Cheng, B.K. Tay, Development of texture in TiN films deposited by filtered cathodic vacuum arc, J. Cryst. Growth. 252 (2003) 257–264, https://doi.org/10.1016/S0022-0248(03)00871-6.
[39] H.S. Park, D.H. Jung, H.D. Na, J.H. Joo, J.J. Lee, The properties of (Ti,Al) N coatings deposited by inductively coupled plasma assisted d.c. magnetron sputtering, Surf. Coat. Technol. 142–144 (2001) 999–1004, https://doi.org/10.1016/S0257-8972(01)01217-8.
[40] T. Hurkmans, D.B. Lewis, H. Paritong, J.S. Brooks, W.D. Münz, Influence of ion bombardment on structure and properties of unbalanced magnetron grown CrNx coatings, Surf. Coat. Technol. 114 (1999) 52–59, https://doi.org/10.1016/S0257-8972(99)00031-6.
[41] H.E. Cheng, M.H. Hon, Texture formation in titanium nitride films prepared by chemical vapor deposition, J. Appl. Phys. 79 (1996) 8047–8053, https://doi.org/10.1063/1.362358.
[42] H.X. Lin, Z.C. Lei, Z.Y. Jiang, C.P. Hou, D.Y. Liu, M.M. Xu, Z.Q. Tian, Z.X. Xie, Supersaturation-dependent surface structure evolution: from ionic, molecular to metallic micro/nanocrystals, J. Am. Chem. Soc. 135 (2013) 9311–9314, https://doi.org/10.1021/ja404371k.
[43] D.G. Vlachos, Growth of elongated nanostructures, Mater. Sci. Eng. A. 204 (1995) 90–95, https://doi.org/10.1016/0921-5093(95)09943-3.
[44] J. Nyvlt, Kinetics of nucleation in solutions, J. Cryst. Growth. 3 (1968) 377–383, https://doi.org/10.1016/0022-0248(81)90380-8.
[45] D. Rafaja, C. Wüstefeld, M. Dopita, M. Motylenko, C. Baehtz, C. Michotte, M. Kathrein, Crystallography of phase transitions in metastable titanium aluminium nitride nanocomposites, Surf. Coat. Technol. 257 (2014) 26–37, https://doi.org/10.1016/j.surfcoat.2014.01.039.
[46] E. Chason, B.W. Sheldon, L.B. Freund, J.A. Floro, S.J. Hearne, Origin of compressive residual stress in polycrystalline thin films, Phys. Rev. Lett. 88 (2002) 4, https://doi.org/10.1103/PhysRevLett.88.156103.
[47] E. Chason, P.R. Guduru, Tutorial: understanding residual stress in polycrystalline thin films through real-time measurements and physical models, J. Appl. Phys. 119 (2016) 191101, https://doi.org/10.1063/1.4949263.
[48] H.Z. Yu, C.V. Thompson, Grain growth and complex stress evolution during Volmer-Weber growth of polycrystalline thin films, Acta Mater. 67 (2014) 189–198, https://doi.org/10.1016/j.actamat.2013.12.031.
[49] T. Michely, J. Krug, Islands, Mounds and Atoms, Springer Science \& Business Media, 2012.
[50] J.H. Huang, Y.H. Chen, A.N. Wang, G.P. Yu, H. Chen, Evaluation of fracture toughness of ZrN hard coatings by internal energy induced cracking method, Surf. Coat. Technol. 258 (2014) 211–218, https://doi.org/10.1016/j.surfcoat.2014.09.026.
[51] A.-N. Wang, G.-P. Yu, J.-H. Huang, Fracture toughness measurement on TiN hard coatings using internal energy induced cracking, Surf. Coati. Technol. 239 (2014) 20–27.
[52] W.M. Seidl, M. Bartosik, S. Kolozsvári, H. Bolvardi, P.H. Mayrhofer, Influence of Ta on the fracture toughness of arc evaporated Ti-Al-N, Vacuum 150 (2018) 24–28.